Medical Physics
The International Journal of Medical Physics Research and Practice

Validation of MTF measurement for digital mammography quality control

Ann-Katherine Carton, Dirk Vandenbroucke, Luc Struye, Andrew D. A. Maidment, Yen-Hong Kao, Michael Albert, Hilde Bosmans, and Guy Marchal

Citation: Medical Physics **32**, 1684 (2005); doi: 10.1118/1.1921667
View online: http://dx.doi.org/10.1118/1.1921667
View Table of Contents: http://scitation.aip.org/content/aapm/journal/medphys/32/6?ver=pdfcov
Published by the American Association of Physicists in Medicine

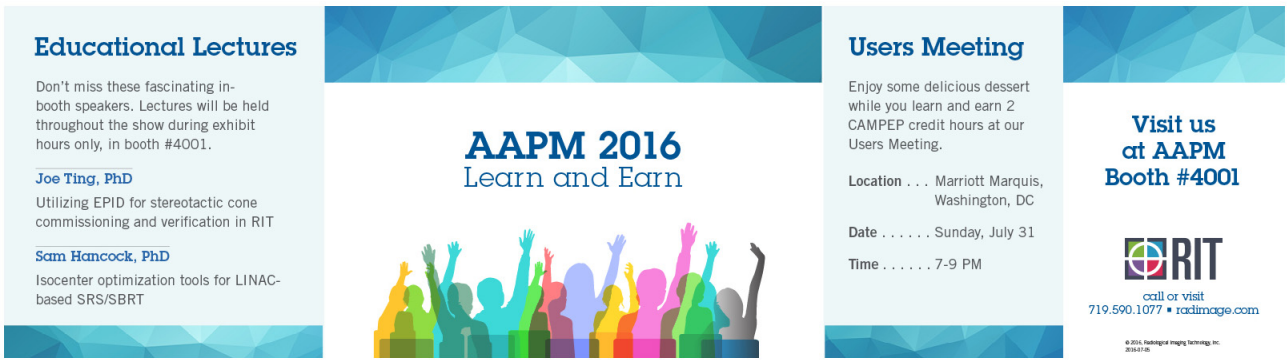

Validation of MTF measurement for digital mammography quality control

Ann-Katherine Carton[a)]
University Hospitals of Leuven, Herestraat 49, Leuven, Brabant 3000, Belgium

Dirk Vandenbroucke and Luc Struye
Agfa-Gevaert, Septestraat 27, B-2640 Mortsel, Belgium

Andrew D. A. Maidment, Yen-Hong Kao, and Michael Albert
Hospital of the University of Pennsylvania, Department of Radiology, Philadelphia, Pennsylvania 19104

Hilde Bosmans and Guy Marchal
University Hospitals of Leuven, Herestraat 49, Leuven, Brabant 3000, Belgium

(Received 19 November 2004; revised 18 March 2005; accepted for publication 31 March 2005; published 24 May 2005)

The modulation transfer function (MTF) describes the spatial resolution properties of imaging systems. In this work, the accuracy of our implementation of the edge method for calculating the presampled MTF was examined. Synthetic edge images with known MTF were used as gold standards for determining the robustness of the edge method. These images simulated realistic data from clinical digital mammography systems, and contained intrinsic system factors that could affect the MTF accuracy, such as noise, scatter, and flat-field nonuniformities. Our algorithm is not influenced by detector dose variations for MTF accuracy up to $1/2$ the sampling frequency. We investigated several methods for noise reduction, including truncating the supersampled line spread function (LSF), windowing the LSF, applying a local exponential fit to the LSF, and applying a monotonic constraint to the supersampled edge spread function. Only the monotonic constraint did not introduce a systematic error; the other methods could result in MTF underestimation. Overall, our edge method consistently computed MTFs which were in good agreement with the true MTF. The edge method was then applied to images from a commercial storage-phosphor based digital mammography system. The calculated MTF was affected by the size (sides of 2.5, 5, or 10 cm) and the composition (lead or tungsten) of the edge device. However, the effects on the MTF were observed only with regard to the low frequency drop (LFD). Scatter nonuniformity was dependent on edge size, and could lead to slight underestimation of LFD. Nevertheless, this negative effect could be minimized by using an edge of 5 cm or larger. An edge composed of lead is susceptible to L-fluorescence, which causes overestimation of the LFD. The results of this work are intended to underline the need for clear guidelines if the MTF is to be given a more crucial role in acceptance tests and routine assessment of digital mammography systems: the MTF algorithm and edge object test tool need to be publicly validated.
[DOI: 10.1118/1.1921667]

Key words: MTF, digital detectors, simulations

I. INTRODUCTION

In a well-designed x-ray imaging system, the properties of the detector are the prime determinant for the apparent resolution in the radiological images. Spatial resolution is one of the parameters that is routinely checked during acceptance procedures and regular quality control measurements of these systems. Both qualitative and quantitative measurement methods are used. Qualitative methods rely on human observations. They include the analysis of line-pair test objects or the determination of visibility thresholds for inserts of different diameter. The modulation transfer function (MTF)[1,2] is a quantitative and direct metric that describes the image resolution properties of a system as a function of the spatial frequency. Automated calculation of the MTF is possible. Both approaches are being considered in physical and technical protocols for quality assurance in digital mammography.[3]

Clinical image resolution is influenced by so many factors that it may be indicated to include both the measurement of the MTF of the detector and the MTF of the complete system in quality assessment protocols for digital mammography. For a system in good working condition, the resolution of the detector has the greatest impact. Other technical determinants include: the focal spot size, the geometry of the system, and the scatter. The x-ray scatter in the breast certainly reduces the intrinsic resolution of the images. Its effect depends, in theory, on the exposure conditions, the compressed breast thickness, and the composition of the breast.

A straightforward way to allow the calculation of the MTF under clinical conditions on a routine basis would be to include an edge test object into a comprehensive test object for digital mammography systems. As far as we know, there is not yet an international consensus regarding possible acquisition methods. The International Electrotechnical Com-

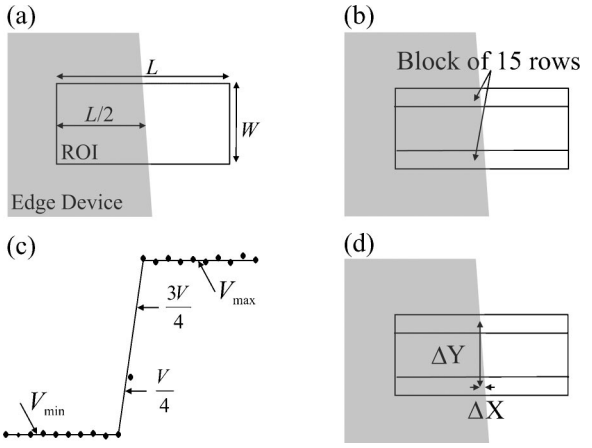

FIG. 1. (a) Geometry of the region of interest (ROI) for the determination of the MTF; (b) selection of two blocks of 15 lines from opposite ends of the ROI as a first step to calculate the edge angle; (c) graph to determine the central position of each row; (d) outline to calculate the edge angle and number of rows to be projected.

mission (IEC)[4] has published a standard for the calculation of the MTF of digital x-ray detectors, excluding digital mammography. Currently, a workgroup of the IEC[5] is focusing on similar methods for MTF calculation of the detector in digital mammography. The scientific literature about the detector MTF,[6–8] including digital mammography,[9–11] is however rapidly growing. The literature about MTFs acquired under clinical conditions is scarce.[12–14] The value and the robustness of MTF calculations under clinical conditions remains to be further validated.

This study is a part of a larger study that aims to describe a new test object for digital mammography quality control in routine clinical practice. In comprehensive test objects there is only limited space available for an edge. In this study, we first assessed the accuracy of various methods to calculate the presampled MTF on synthetic images that include noise, scatter, and flat-field inhomogeneities. We then exposed edges of different sizes and composition to explore how accurate MTF measurements of digital mammography systems can be acquired.

II. MATERIAL AND METHODS

A. Basic MTF algorithm

Described in the following is the algorithm used to compute the MTF. This algorithm requires an image of a slightly tilted edge (typically 1°–3° with respect to the pixel matrix). The signal intensities in the image must be linear with detector dose.

Step 1: A region of interest (ROI) centered around the edge is selected. This ROI is defined by a width W and a length L [Fig. 1(a)]. W is the total number of rows used for the determination of the MTF. L is the length of the edge profiles.

Step 2: Two blocks of rows each consisting of 15 rows are selected from the edge image; these blocks are selected from opposite ends of the ROI [Fig. 1(b)]. For each row the central position of the edge is determined by (a) applying a low-pass filter to the row profile; (b) calculating $V_{\min}$, the average value of the pixels shielded by the edge, and $V_{\max}$, the average value of the remaining pixels; (c) calculating the mean pixel value of those pixels which have values lying between $(V/4+V_{\min})$ and $(3V/4+V_{\min})$ where $V=V_{\max}-V_{\min}$ [Fig. 1(c)]; and (d) determining the edge position corresponding to this mean pixel value. For each block the average of the 15 edge positions is calculated. From these average edge positions, the edge angle and the corresponding number of lines to be projected in the supersampling procedure, $N_{\text{proj}}=\Delta Y/\Delta X$, is determined by ΔY, the distance between the upper and the lower block, and ΔX [Fig. 1(d)], the difference of the mean pixel locations. N_{proj} is rounded to the nearest integer, N.

Step 3: A supersampled edge spread function (ESF) is generated by using the pixel values of N consecutive rows across the edge: the value of the first pixel in the first row gives the first data point in the supersampled ESF; the first pixel in the second row gives the second data point, etc.; and finally the first pixel in the Nth row gives the Nth data point. This procedure is repeated for the other pixels in the N rows: the value of the first pixel in the second row gives the $(N+1)$th data point; the second pixel in the second row the $(N+2)$th data point, etc. It is assumed that the sampling distance in the supersampled ESF is constant and is given by the pixel spacing divided by N. Slight shifts introduced by this method are equivalent to the binning process of other algorithms.

Step 4: Step 3 is repeated for all other nonoverlapping groups of N-consecutive rows along the edge, thus producing a set of individual supersampled ESFs.

Step 5: A mean supersampled ESF is determined by averaging the individual ESFs; the edge location of each supersampled ESF is estimated by means of linear regression using the ESF data lying between 30% and 70% on the edge transition. The individual supersampled ESFs are laterally shifted such that individual edge positions agree, and finally the supersampled ESFs are averaged.

Step 6: The line spread function (LSF) is calculated by finite-element differentiation of the ESF using a convolution filter with a $[-1\ 1]$ kernel.

Step 7: The modulus of the Fourier transform of the LSF is calculated, the result is normalized to its zero frequency value $[\text{MTF}(0)=1]$.

Step 8: The frequency axis is corrected for the sampling scaling error caused by the slanted edge (the frequency axis is scaled by a factor of $1/\cos\theta$).

Step 9: A third-order low-pass filter is applied to the MTF, starting from the 13th point at which the MTF was estimated, to reduce the noise content. To avoid distortion of the MTF, the filter is applied twice. A copy of the raw MTF data is made. On one array the algorithm is applied from point 13 to the end. On the second array the algorithm is applied in reverse from the last point to point 13. The average of the two filtered MTF curves is calculated.

Step 10: A second normalization is performed to reduce

the apparent noise in the MTF. The best line through the first 7 points is calculated by using linear regression. The MTF curve is normalized again using the *y*-axis intercept of the linear regression.

B. Image simulations

Images were simulated in MATLAB (version 5.3.0, Mathworks, Natick, MA). The images were 1 K by 1 K, 16 bit, with 100 μm pixels. They were simulated with features observed in images acquired with four FFDM systems, including two flat-panel detectors and two storage-phosphor computed radiography (CR) systems. The flat-panel systems included a Senographe 2000D (GE, Milwaukee, WI) with 100 μm pixels and an Embrace DM1000 (Agfa, Mortsel, Belgium) with 70 μm pixels. The first CR system was a FCR 5000 MA (Fuji Medical Systems, Tokyo, Japan). HR-BD plates (Fuji Medical Systems, Tokyo, Japan) were exposed with a Mammomat 3000 (Siemens, Erlangen, Germany) and processed with a FCR PROFECT CS dual-sided reader with 50 μm pixels (Fuji Medical Systems, Tokyo, Japan). The second CR system consisted of a prototype storage-phosphor plate, Embrace 1.0 (Agfa, Mortsel, Belgium), exposed with a M-IV Platinum (Lorad, Danbury, CT) and processed with a Compact Plus single-sided reader with 100 μm pixels (Agfa, Mortsel, Belgium).

1. Simulation of the edge

We first simulated a basic digital edge image, EDGE_B. EDGE_B represents the image of an edge object acquired without scatter or quantum noise by a detector which does not introduce any noise or blurring. The theoretical presampled MTF of EDGE_B is a sinc, fully determined by the pixel size of the detector elements. For this example, we presume a pixel with width w and height h, both equal to 100 μm. EDGE_B was simulated line-by-line using a normalized edge profile $\mathrm{ESF}_B(x)$, where x is the displacement of the edge from the center of the detector element. An angle $\theta = 2°$ to the matrix array[5] was simulated by shifting the edge profiles in each adjacent line by $\Delta x = w \tan\theta$. The signal intensity in each pixel is proportional to the area covered by the edge object. Five regions were used to distinguish the edge object position relative to the pixel matrix (Fig. 2).

For $x < x_1$ the pixel is completely covered by the edge object. So:

$$\mathrm{ESF}_B(x) = 0. \tag{1}$$

For $x_1 < x < x_2$, a triangular region of the pixel is progressively uncovered. The region grows quadratically with x:

$$\mathrm{ESF}_B(x) = \frac{(x - x_1)^2}{(x_2 - x_1)^2}(0.5 \tan\theta). \tag{2}$$

For $x_2 < x < x_3$ a trapezoidal region of the pixel is progressively uncovered:

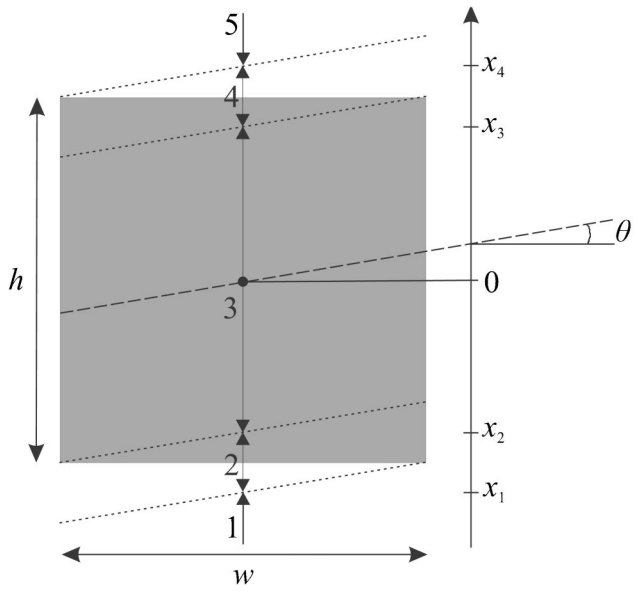

FIG. 2. The position x of the edge is measured along one axis from the center of a pixel. The ESF for EDGE_B can be expressed piecewise as a polynomial in each of the five x intervals shown (dotted lines). The edge angle θ is exaggerated here for clarity.

$$\mathrm{ESF}_B(x) = 0.5 \tan\theta + \frac{x - x_2}{x_3 - x_2}(1 - \tan\theta). \tag{3}$$

For $x_3 < x < x_4$ another triangular region of the pixel is progressively uncovered (basically the same as the first one, but in reverse):

$$\mathrm{ESF}_B(x) = 1 - \frac{(x - x_4)^2}{(x_3 - x_4)^2}(0.5 \tan\theta). \tag{4}$$

For $x > x_4$ the full pixel is uncovered:

$$\mathrm{ESF}_B(x) = 1. \tag{5}$$

From the geometry depicted in Fig. 2, we find:

$$x_1 = 0.5(-h - w \tan\theta), \tag{6}$$

$$x_2 = 0.5(-h + w \tan\theta), \tag{7}$$

$$x_3 = 0.5(h - w \tan\theta), \tag{8}$$

$$x_4 = 0.5(h + w \tan\theta). \tag{9}$$

The supersampled LSF calculated from the supersampled ESF described in Eqs. (1)–(5) is not a simple rectangular function. Instead it ramps up between x_1 and x_2, then is constant between x_2 and x_3, and finally ramps down between x_3 and x_4. This is the convolution of a rectangular function of length h with a rectangular function with length $x_2 - x_1$.

The height of the edge transition is derived from the x-ray transmission of a 30 μm-thick Pb (99.9% purity) edge on top of 40 mm PMMA exposed with 28 kVp, Mo/Mo (25 μm filter). We measured an x-ray transmission (8) of 10.5%. The signal intensities in EDGE_B were then scaled to the final signal intensities.

2. Noise

Real images always include noise both of quantum origin and from the detector. We corrupted the basic image, $EDGE_B$, with noise to yield the image $EDGE_{B_N}$. We generated colored noise $N_C(x,y)$ characterized by a rotationally symmetric normalized noise power spectra $NNPS_C(u,v)$ with shape similar to the horizontal NNPS of the Agfa Embrace 1.0 CR plate. The assumption of rotational symmetry is a simplification; however, the response of the CR plates does not differ dramatically for other directions. The noise $N_C(x,y)$ was simulated based on the method described by Bochud[15] as

$$N_C(x,y) = \text{real}(\mathfrak{F}_2^{-1}\{\sqrt{NNPS_C(u,v)} \cdot e^{i\Phi_W(u,v)}\}), \quad (10)$$

where $\mathfrak{F}_2^{-1}$ is the two-dimensional inverse Fourier transform and $\Phi_W(u,v)$ is the randomly distributed phase ($\Phi_W \in [-\pi,\pi]$) of a Gausian white noise spectrum.

We simulated different noise levels for the part of the image containing the edge, the part without the edge, and the transition zone. We assumed that $NNPC_C(u,v)$ has the same shape independent of dose, which shows close agreement with reality for the examined dose range. A linear relationship exists between the variance of the noise in the image space and the level of the $NNPS_C(u,v)$. In addition, the relationship between the average signal intensity (I) and noise variance, $\sigma^2(I)$, was determined experimentally from linearized images of the Agfa Embrace 1.0 CR system (Fig. 3). To do so, we exposed 40 mm of PMMA on top of the bucky at 28 kVp and various exposure levels.

The noise in the edge image, $EDGE_B$, was then simulated using $N_{Cnorm}(x,y)$,

$$N_{Cnorm}(x,y) = \alpha\, N_C(x,y) - \beta, \quad (11)$$

where α and β were chosen so that $N_{Cnorm}(x,y)$ had a mean of 0 and a variance of 1. Thus:

$$EDGE_{B_N}(x,y) = N_{Cnorm}(x,y) \cdot \sigma(I) + EDGE_B(x,y). \quad (12)$$

We simulated $EDGE_{B_N}$ with detector doses of 1.8 mR (~SNR=17.1 dB), 5.6 mR (~SNR=19 dB), 11.7 mR (~SNR=19.8 dB) in the plane of the detector that would be acquired when exposing 40 mm PMMA at 28 kVp with Mo/Mo without the edge test object.

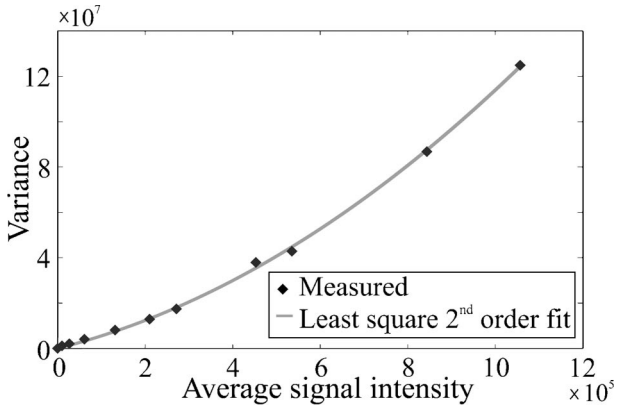

FIG. 3. Relationship between average signal intensity and noise variance in images acquired with a prototype Agfa CR plate with 100 μm pixels. The images of 40 mm PMMA were exposed at 28 kVp, Mo/Mo at different exposure settings.

We ignored fixed pattern noise. We assumed that for the purpose of these simulations, the incorporation of this noise source would not have an apparent effect on the complete noise pattern.

3. Scatter

X-ray scatter, beam hardening, K-fluorescence, reabsorption in the detector, and scattering of light photons are possible causes of a low frequency drop (LFD) in MTF measurements.[14] Shen *et al.*[14] found a LFD to be larger when adding more scattering material to the x-ray field. Rogge *et al.*[13] observed the same phenomena.

For our simulations, we measured the MTF(f) of an edge centered within 60 mm PMMA and exposed with the GE flat-panel at 28 kVp, Mo/Mo. This MTF shows a large LFD (0.77 at 0.5 mm^{-1}). We evaluated a model, $MTF_{LFD}(f)$, combining two Lorentzian functions at all spatial frequencies f, as this has previously shown to fit experimental measurements:[11,13,16]

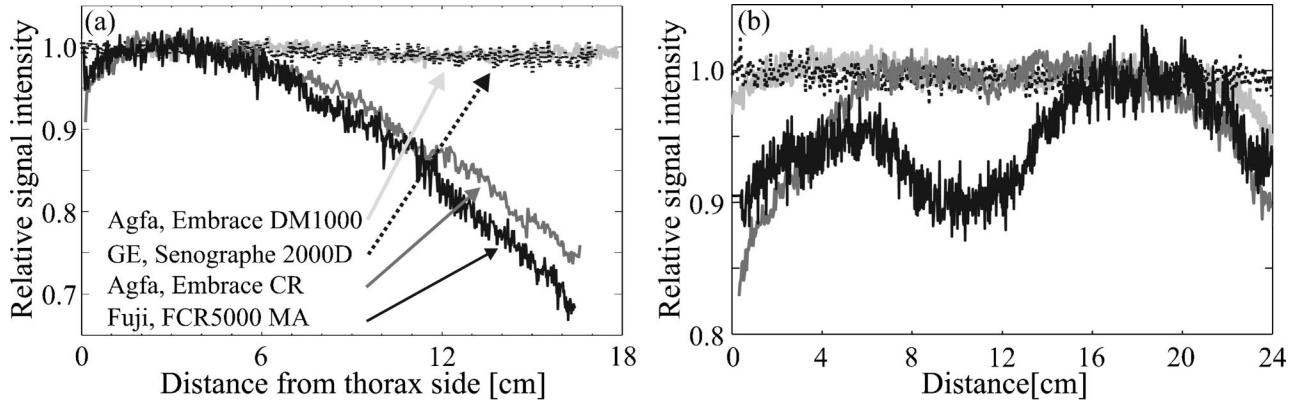

FIG. 4. Demonstration of flat-field nonuniformities. The relative signal intensities (a) along the central axis perpendicular to the chest wall side and (b) parallel to and 6 cm from the chest wall side are shown for 4 FFDM systems. All measurements are for exposures at 28 kVp with Mo/Mo and 40 mm PMMA.

$$\mathrm{MTF}_{\mathrm{LFD}}(f) = \frac{a}{1+\left(\frac{f}{b}\right)^2} + \frac{1-a}{1+\left(\frac{f}{c}\right)^2}, \quad (13)$$

where a, b, and c are parameters with $a \in [0,1]$, $b > 0$ (mm^{-1}) and $c > 0$ (mm^{-1}). The parameters were determined by minimizing the sum of the squared differences between the model and the measured data. We found $a = 0.224$, $b = 0.045$ mm^{-1}, and $c = 3.807$ mm^{-1}.

An edge image EDGE_{LFD} with the above-noted MTF_{LFD} was simulated. EDGE_{LFD} was filled line-by-line using the edge profile $\mathrm{ESF}_{LFD}(x)$:

$$\mathrm{EDGE}_{LFD}(x) = a(2 - e^{2\pi bx}) + (1-a)(2 - e^{2\pi cx}) \quad \text{for } x < 0,$$

$$\mathrm{EDGE}_{LFD}(x) = ae^{-2\pi bx} + (1-a)e^{-2\pi cx} \quad \text{for } x > 0. \quad (14)$$

To simulate an edge with an edge angle of $\theta = 2°$ with respect to the pixel matrix, the adjacent lines were shifted with $\Delta x = w \tan\theta$.

Next, noise was added to EDGE_{LFD} as explained in Sec. II B 2, which then results in EDGE_{LFD_N}. We simulated EDGE_{LFD_N} corresponding to a detector dose of 5.6 mR.

4. Flat-field inhomogeneities

Several effects contribute to radiation field nonuniformities: the heel effect along the anode–cathode axis, the inverse square law, and differential photon-path lengths through various attenuating media (the Be window of the x-ray tube, the added filtration, the mirror, and the compression paddle).[17] The angle of incidence in detector elements may also play a role. The most apparent nonuniformity is the heel effect along the anode–cathode axis. The images of a DR system are usually flat-field corrected whereas images of current CR systems are not. To simulate flat-field nonuniformities, we measured the signal intensities as a function of position in the four FFDM systems. The systems were exposed at 28 kVp and Mo/Mo with 40 mm PMMA on top of the bucky. Figure 4(a) plots the relative signal intensity along the central axis, perpendicular to the chest wall side. Figure 4(b) shows the relative signal intensity parallel to the chest wall side of the detectors, 6 cm from the chest wall.

We decided to model flat-field inhomogeneities as observed in images from the Fuji CR system. We fitted a fourth-order polynomial through the profile parallel to the anode–cathode axis and a second-order polynomial through the profile perpendicular to the anode–cathode axis. Two images were made to separately show the influence of the vertical and horizontal nonuniformities: EDGE_{LFD_V} and EDGE_{LFD_H} where "*V*" represents the nonuniformity perpendicular to the anode–cathode axis and "*H*" represent the nonuniformity along the anode–cathode axis. Noise was then inserted as described earlier. This resulted in $\mathrm{EDGE}_{LFD_{N_V}}$ and $\mathrm{EDGE}_{LFD_{N_H}}$. We simulated a detector dose of 5.6 mR.

C. Application of the MTF tools in real images

In reality, edge objects necessarily have a finite size. As x rays propagate through a phantom composed of an edge object placed within PMMA, the distribution of the scattered x rays will be different in the open field of the PMMA, in the open PMMA field near the edge, under the edge object near the edge, and in the center of the edge object. The spatial distribution of the scatter also depends on the edge object material. An individual edge profile is influenced by the distance between the position of the profile and the other borders of the test object. The accuracy of the MTF may be degraded if the region for the calculation of the supersampled ESF is affected by scatter from the borders. Experiments with edge objects of different sizes were performed to verify the accuracy of MTF calculations from (potentially small) edge test objects inserted in a comprehensive phantom for quality control in digital mammography. Measurements

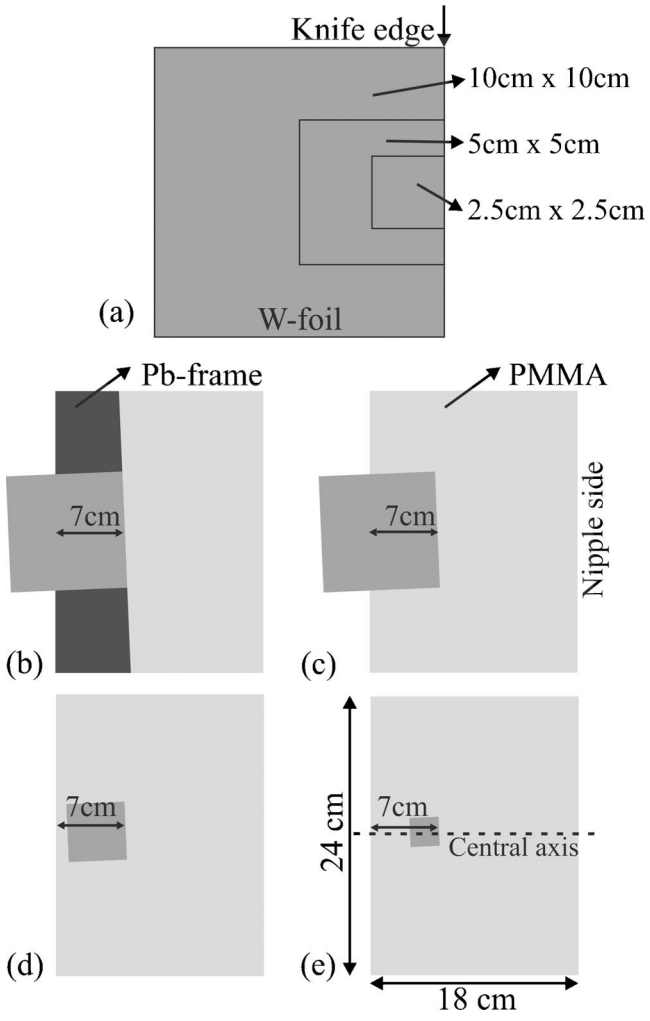

FIG. 5. Edge device placement. (a) W foil used in the MTF experiments. The lines show how the 10 cm × 10 cm W foil was cut into squares with sides of 5 and 2.5 cm. (b), (c), (d), and (e) Top view of acquisition geometry of the five edge devices: (b) 10 cm × 10 cm W foil with a Pb frame; (c) 10 cm × 10 cm W foil; (d) 5 cm × 5 cm W foil and 5 cm × 5 cm Pb foil; (e) 2.5 cm × 2.5 cm W foil. The 2° angle is exaggerated for clarity.

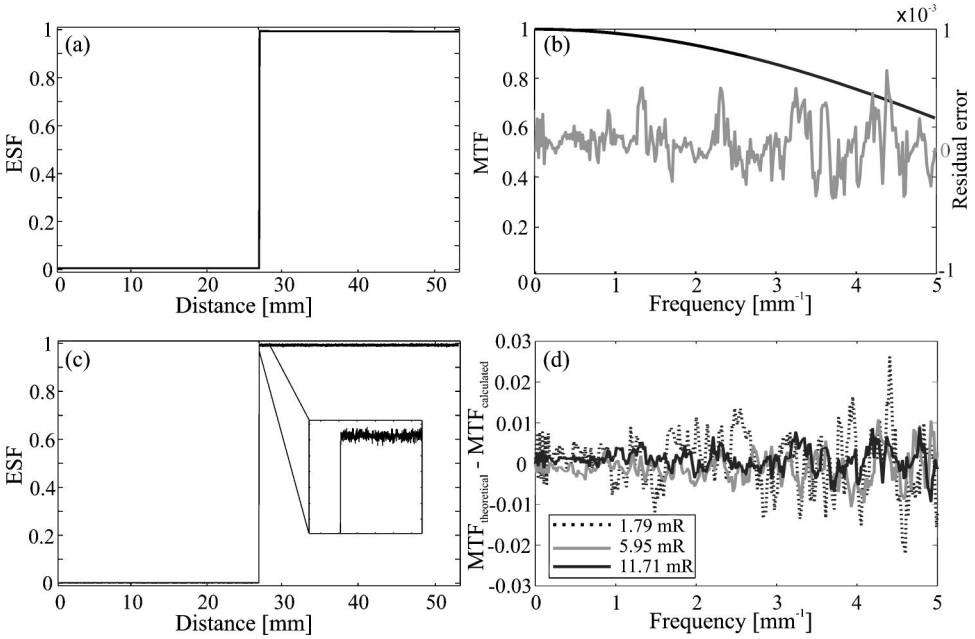

FIG. 6. (a) and (b) demonstrate the supersampled ESF_B and MTF (theoretical and calculated) from an edge object acquired with a noiseless and spatially uniform detector. (c) and (d) The influence of detector noise. (c) A normalized supersampled ESF_{B_N} at 5.6 mR. The difference between the theoretical MTF and the calculated MTF is shown in (d).

with edge objects of different composition were performed to explore the influence of the composition on MTF measurements.

Five edge test devices were evaluated. Four of the five edges consisted of a 127-μm-thick, 99.9% pure W foil (Sigma-Aldrich, Germany) laminated between two 1-mm-thick PMMA slabs. The PMMA slabs covered the entire field of the detector surface. The first edge device consisted of a 10 cm by 10 cm W foil windowed by a 200-μm-thick Pb plate which were laminated between two 1-mm-thick PMMA slabs. The Pb plate covered the entire length of the detector and was suitable to prevent scatter at the sides of the W foil. The second edge device consisted of a W foil without a Pb window. For the third and fourth edge devices, the W foil was cut first to a square with 5 cm sides and then to a square with 2.5 cm sides. The W foil was cut so that the same part of the knife edge was always used for the determination of the MTF [Fig. 5(a)]. The acquisition geometries are schematically illustrated in Figs. 5(b)–5(e). The W foils were aligned to the central anode–cathode axis. The knife edges all intersected the x-ray field at 7 cm from the thorax side. The angle of the knife edge with respect to the pixel matrix was approximately 2°. The fifth edge consisted of a 30-μm-thick, 99.9% pure square Pb foil with sides of 5 cm (Hüttner Röntgenteste, Germany) which was also laminated between two 1-mm-thick PMMA slabs that covered the entire field of the detector. The same geometric setup was used as for the other four edge objects. During image acquisition, the five edge devices were each placed within two additional 20 mm PMMA slabs.

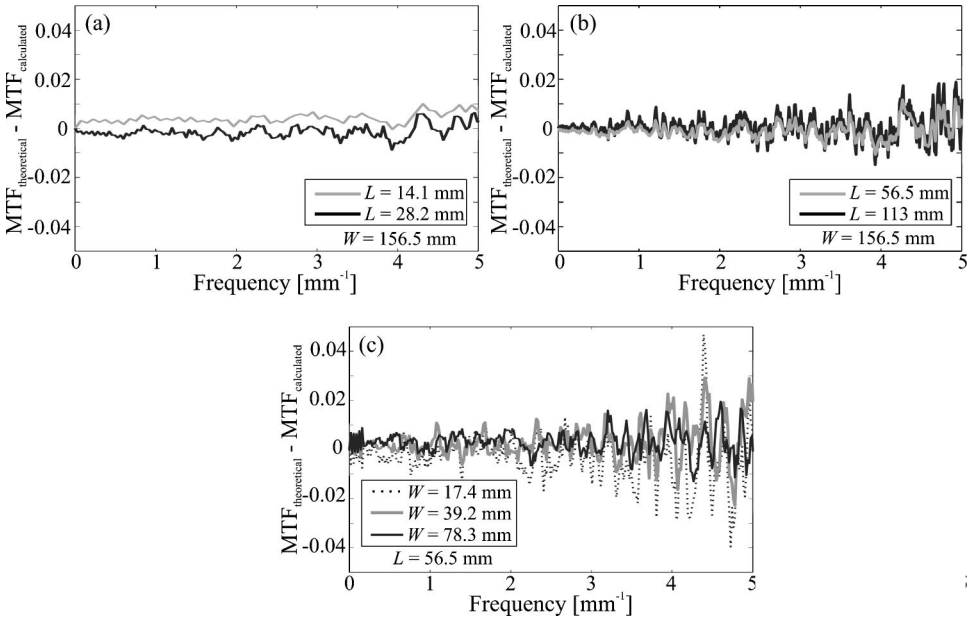

FIG. 7. Effect of length L, of the supersampled ESF_{B_N} on MTF accuracy is shown in (a) and (b). Effect of W on MTF accuracy is shown in (c). The difference between the theoretical MTF and calculated MTF is shown. Smaller L and larger W reduce the noise content of the MTF.

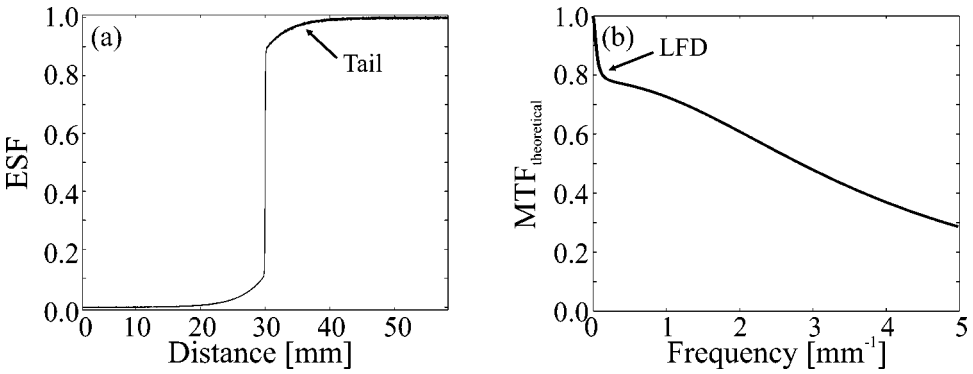

FIG. 8. (a) Example of a normalized supersampled ESF_{LFD_N} computed from $EDGE_{LFD_N}$, a simulated edge corrupted by noise and scatter. (b) The theoretical MTF from $EDGE_{LFD_N}$.

Images of the edge test devices were acquired using 28 kVp, Mo/Mo with the Agfa CR system at a detector dose of approximately 5.6 mR. These image data are square-root compressed.[18] Therefore, we squared the image data to get signal intensities in the images that are linearly related with dose. The images were flat-fielded using a correction template derived from a flat-field image acquired under the same experimental conditions as the edge test device images. The Fourier transform of this flat-field image was high-pass filtered. The inverse Fourier transform produced the template for correcting the nonuniform edge image. MTFs were calculated with the method described in Sec. II A. The MTF calculated from the image of the W foil fixed in the Pb plate was taken as a reference. The spatial scatter distribution received throughout the whole edge object will be theoretically constant, with the exception of the region adjacent to the knife edge. The MTFs calculated from the images of the smaller W foils were compared with this reference MTF. The MTF calculated from the image of the Pb-edge device was also compared with the reference MTF.

III. RESULTS

A. Validation of the MTF tool on simulated data

Figure 6(a) shows the normalized supersampled ESF obtained by applying the MTF algorithm on the image $EDGE_B$. The supersampled ESF was derived from a ROI with $L=56.5$ mm and $W=156.5$ mm. Figure 6(b) shows the corresponding theoretical MTF and the MTF calculated with our method. There is very good agreement between theory and our calculations as shown by the residual. The maximum absolute difference up to 5 mm^{-1} is only 0.06%.

Next, we evaluated the supersampled ESFs as derived from images with different noise levels: $EDGE_{B_N}$. As described in Sec. II B 2, images were simulated for detector doses of 1.8, 5.6, and 11.7 mR. The ESFs were derived from ROIs with $L=56.5$ mm and width $W=156.6$ mm. Figure 6(c) is an example of a supersampled ESF at 5.6 mR detector dose. Figure 6(d) shows the difference between the true MTF and the MTFs calculated for the three simulated images with different dose levels. The MTFs are proportionally affected by noise; the influence of the noise is more notable at lower doses. Note that for the first 13 points of the MTF (in this instance below 0.5 mm^{-1}), the noise in the calculated MTF is larger, as the low pass filter (step 9 in Sec. II A) is not applied to these points. The MTF is also noisier at higher spatial frequencies. The absolute difference between the theoretical and the calculated MTFs are smaller than 3% and no appreciable bias is observed. We believe that this can be explained by the fact that we applied $|\mathfrak{F}\{\langle \mathrm{ESF_i}\rangle\}|$ rather than $\langle|\mathfrak{F}\{\mathrm{ESF}_i\}|\rangle$. The angular brackets $\langle\cdots\rangle$ express average values.

The magnitude of the noise depends on the length L of the ESF and on the number of nonoverlapping groups that are averaged, which is determined by W. Figures 7(a) and 7(b) show the MTFs determined from $EDGE_{B_N}$ (corresponding to a detector dose of 5.6 mR) using different lengths L of the ESF of 14.1, 28.2, 56.5, and 113 mm. W was kept constant and equals 156.5 mm. It has been reported that truncation of the tails can reduce the noise content of the MTF,[19] an effect that is also seen here. Figure 7(c) shows the MTF determined from $EDGE_{B_N}$ (corresponding to a detector dose of 5.6 mR) using different widths W of the ESF: 17.4, 39.2, and 78.3 mm. L was kept constant and equals 56.5 mm. In our algorithm, the use of larger W results in averaging over more supersampled ESFs, which has the same effect as measuring the MTF at a higher exposure level and thus reduces the noise.

The remaining calculations are performed on simulated edge images corresponding to a 5.6 mR detector dose, as this

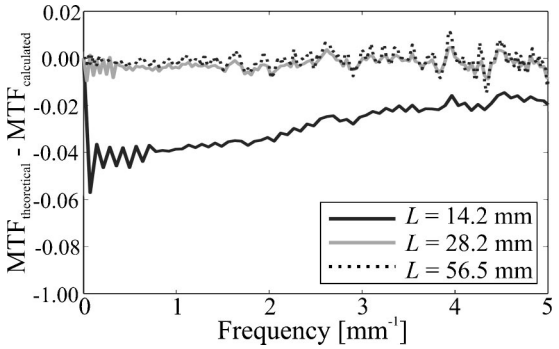

FIG. 9. Effect of the length, L, of the supersampled ESF_{LFD_N} on MTF accuracy. The width W of the ROI was kept constant and equals 156.5 mm. The differences between the theoretical MTF and calculated MTFs determined from $EDGE_{LFD_N}$, a simulated edge corrupted by noise and scatter, are shown.

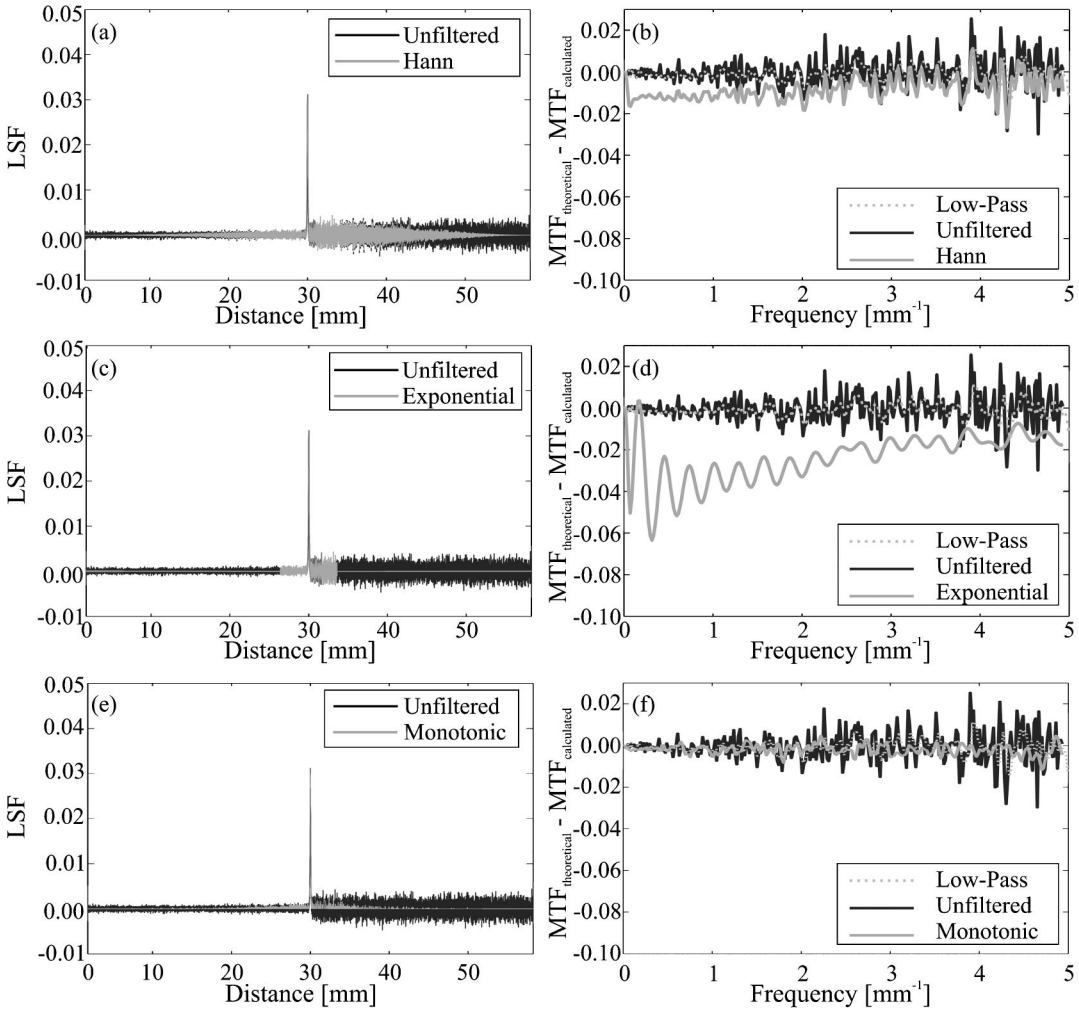

FIG. 10. Effect of noise reduction methods on MTF accuracy. (a), (c), and (e) Supersampled LSF_{LFD_N} (Unfiltered) computed from a simulated edge corrupted by noise and scatter. (a) The LSF_{LFD_N} after applying a Hann window with length equal to the distance between the end points of LSF_{LFD_N}. (c) The LSF_{LFD_N} after truncating the tails at ±3.5 mm and applying exponential extrapolation from ±3.5 toward ±28.25 mm. (e) The LSF_{LFD_N} after having applied a monotonic criterion to the supersampled ESF_{LFD_N}. (b), (d), and (f) Differences between the theoretical MTF and computed MTF from $EDGE_{LFD_N}$ for the three methods. The curve "Low-pass" illustrates the influence including the low-pass filter. The low-pass filter was not used for the curves labeled "Hann," "Exponential," "Monotonic," and "Unfiltered."

dose corresponds to a typical clinical exposure. We analyzed the effect of scattered x rays on the MTF calculation. The tails of the supersampled ESF are greatly affected by the scatter component. Figure 8 shows the supersampled ESF and corresponding theoretical MTF of an image with simulated scatter and noise, $EDGE_{LFD_N}$. The supersampled ESF_{LFD_N} was derived from a ROI with $L=56.5$ mm and $W=156.5$ mm. Figure 9 illustrates the MTFs computed from ESF_{LFD_N} with three different lengths L: 14.1, 28.2, and 56.5 mm. The width W of the ROI to determine ESF_{LFD_N} was set equal to 156.5 mm. The difference between the theoretical and the computed MTF is greater at low frequencies and for smaller values of L. A 56.5-mm-long supersampled ESF_{LFD_N} seems an appropriate choice, because the maximum absolute difference below 1 mm^{-1} is only 0.4%.

The discontinuity at the ends of the tails of a supersampled LSF may introduce the Gibbs effect in the MTF (not seen in the above-noted examples). This behavior is most pronounced when the discontinuity is large. Applying a window function removes the discontinuity at the ends of the supersampled LSF and reduces the Gibbs effect. Moreover, use of a window reduces the noise content in the MTF. For these two reasons some MTF calculation procedures apply a window function.[7,9] However, the improvement comes at a cost: reduced accuracy of the MTF. As an example, we use a Hann window. Figure 10(a) illustrates LSF_{LFD_N} with and without the window. Figure 10(b) plots the difference between the theoretical MTF and the computed MTFs with and without applying a Hann window. This calculation was performed without the low-pass filter (step 9 in Sec. II A). Figure 10(b) also demonstrates the difference between the theoretical MTF and the computed MTFs as calculated with our method, i.e., with the low-pass filter. The noise reduction obtained by applying the Hann window is similar to that

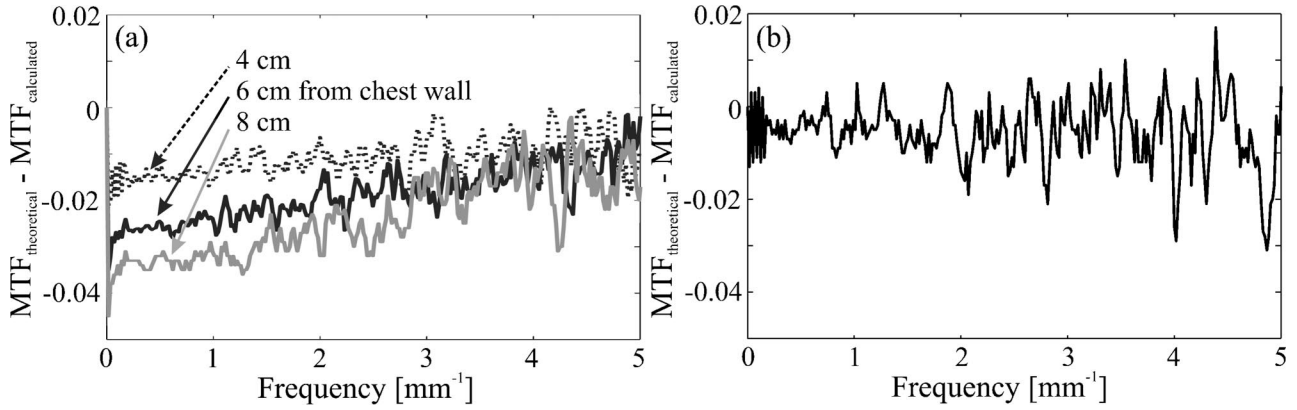

FIG. 11. Effect of flat-field nonuniformities, as measured in images of the Fuji CR system, on MTF accuracy. The differences between the theoretical MTF and calculated MTFs determined from $EDGE_{LFD_{N_H}}$, a simulated edge corrupted by noise and scatter, are shown. (a) The effect of nonuniformity in anode–cathode direction at various distances from the chest wall (b) parallel to the chest wall.

which we get when applying the low-pass filter (step 9) to the MTF. However, the use of the Hann window introduces a systematic overestimation of the MTF. In the present example, the maximum absolute difference is 1.6% at 0.05 mm^{-1}. The maximum absolute difference is greater when a window with a smaller aperture is applied (not shown here).

Other techniques[6,9,19,20] are also frequently used to reduce the noise content in MTF calculations. We restrict ourselves to two methods. One possible approach that can be used is to fit the tails of the LSF to a model.[19] As an example, we exponentially extrapolate the truncated tails of the 56.5 mm supersampled ESF calculated from $EDGE_{LFD_N}$ [Fig. 10(c)]. Figure 10(d) shows the difference between the theoretical MTF and the measured MTF with and without exponential extrapolation. We show the difference calculated with and without the low pass filter (step 9 in Sec. II A). For frequencies >2 mm^{-1}, the noise reduction by applying the exponential extrapolation is similar to the reduction we get when we apply the low-pass filter (step 9 under Sec. II A). The LFD is underestimated: 6.3% at 0.3 mm^{-1}. Notable Gibbs ringing is introduced because of the discontinuity between the measured and the fitted model.

A second possible method to reduce MTF noise is based upon imposing the constraint that the supersampled ESF is monotonic.[9] The supersampled ESF calculated from $EDGE_{LFD_N}$ is shown in Fig. 10(e). Figure 10(f) shows the difference between the theoretical MTF and the measured MTF. The LFD is not overestimated and the noise content is reduced.

Differences in MTF accuracy were also investigated as a function of position in the detector field. We applied our MTF algorithm to edge images with flat-field inhomogeneities, $EDGE_{LFD_{N_H}}$ and $EDGE_{LFD_{N_V}}$, as described earlier. The $EDGE_{LFD_{N_H}}$ was simulated for three different edge positions: at 4, 6, and 8 cm from the thorax side. Figure 11 is a plot of the difference between the true MTF and the calculated MTFs from edge images with flat-field nonuniformities. They were calculated from supersampled ESFs with width $W=156$ mm and length $L=56.5$ mm. The inhomogeneity of the x-ray beam in the anode–cathode direction results in an overestimation of the MTF. This effect is greatest at (4.5% at 0.02 mm^{-1}) 8 cm from the thorax side [Fig. 11(a)]. Only a minor increase (0.4%) is noted for the effect parallel with the thorax side [Fig. 11(b)].

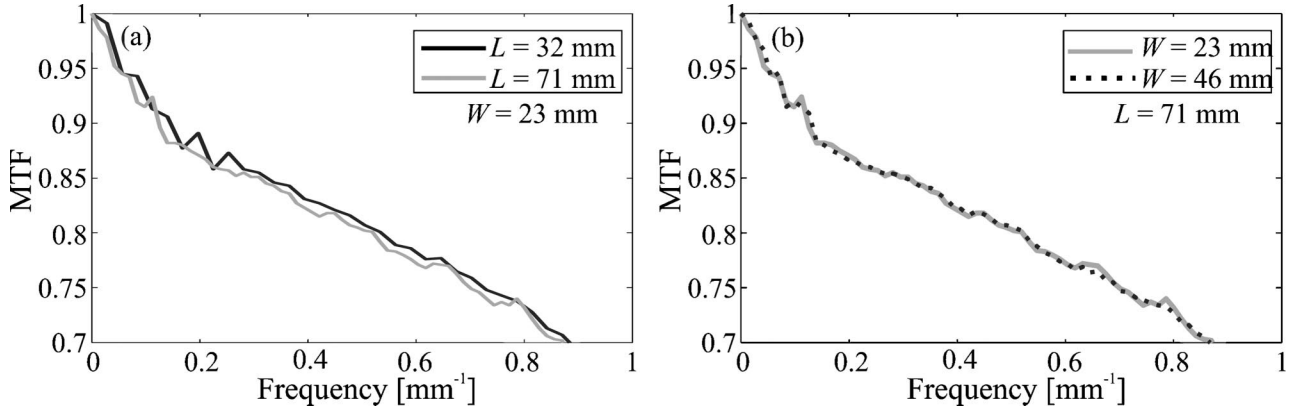

FIG. 12. (a) Effect on estimated MTF due to the length, L, of the super-sampled ESF, (b) width, W. The edge device consisted of a 10 cm by 10 cm W foil windowed by a Pb plate.

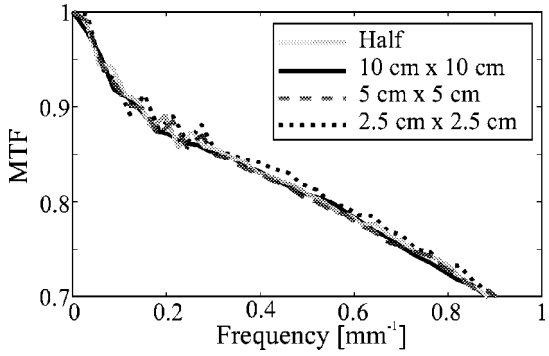

FIG. 13. Effect of scatter nonuniformity on the MTF. MTFs are shown from edge devices with different spatial extent: the 10 cm by 10 cm W foil with Pb frame (half), the 10 cm by 10 cm W foil without Pb frame, the 5 cm by 5 cm W foil, the 2.5 cm by 2.5 cm W foil. The ROIs to determine the supersampled ESF had length $L=32$ mm and width $W=23$ mm.

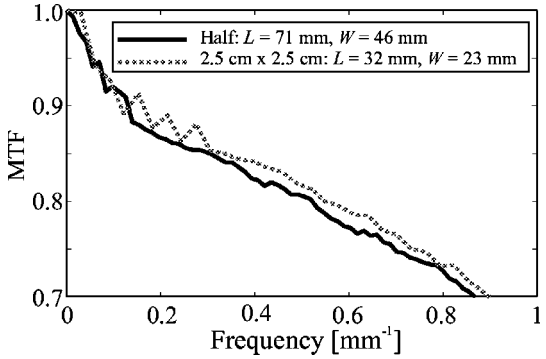

FIG. 14. Combined effect of the length, L, of the supersampled ESF and nonuniform scatter on MTF. The measured MTFs of the edge device consisting of the 10 cm by 10 cm W foil with Pb window ("Half") (ROI: $L=71$ mm, $W=46$ mm) and the 2.5 cm by 2.5 cm W foil (ROI: $L=32$ mm, $W=46$ mm) are shown. Zoom shows the LFD.

B. Application of the MTF tool in real images

To evaluate the effect of the length, L, of the ROI, we calculated the MTF from the 10 cm by 10 cm W-foil edge device windowed by the Pb plate with $L=23$ mm and $L=71$ mm, and $W=32$ mm. Overall, the two MTFs are very similar. The imaging system demonstrates a notable LFD. Figure 12(a) shows the effect on the LFD. In the case of the longer supersampled ESF, the LFD is slightly greater (on average 0.7% up to 1 mm^{-1}).

To evaluate the effect of the width, W, of the ROI of the supersampled ESF, we calculated the MTF from the 10 cm by 10 cm W-foil edge device windowed by the Pb plate with $W=23$ mm and $W=46$ mm, and $L=71$ mm [Fig. 12(b)]. No systematic difference is observed over the whole frequency range.

To evaluate the effect of scatter nonuniformity over the ROI, we calculated the MTF from the 10 cm by 10 cm W-foil edge device windowed by the Pb plate, the 10 cm by 10 cm W-foil edge device alone, the 5 cm by 5 cm W-foil edge, and the 2.5 cm by 2.5 cm W-foil device using $L=32$ mm and $W=23$ mm. We see in Fig. 13 that the MTF from the 2.5 cm by 2.5 cm W-foil edge appears to have a slightly smaller LFD (on average 0.7% up to 1 mm^{-1}). We believe that this is due to the nonuniformity of the scatter intensity across the ROI.

To evaluate the combined effect of the length, L, of the ROI with nonuniform scatter, we calculated the MTF with the 10 cm by 10 cm W-foil edge device windowed by the Pb plate using $L=71$ mm, $W=46$ mm and the 2.5 cm by 2.5 cm W-foil edge device using $L=32$ mm, $W=23$ mm (Fig. 14). The MTFs are very similar overall, differing no more than 1.4% at frequencies up to 1 mm^{-1}.

To evaluate the effect of the edge material, we calculated the MTFs from the 5 cm by 5 cm W-foil edge device and the 5 cm by 5 cm Pb-foil edge device using $L=71$ mm and $W=46$ mm [Fig. 15(a)]. The MTF measured with the Pb foil shows a slightly smaller MTF in the low frequency range (up to 1.3% at 0.33 mm^{-1}) [Fig. 15(b)]. This degradation may be due to fluorescent x rays, as the L-edge of Pb is around 16 keV.

IV. DISCUSSION AND CONCLUSIONS

In this study, we explored the accuracy of a supersampled edge MTF measurement method for frequencies up to 1/2 the sampling frequency. We claim that this method is the only practical method for which a sufficiently accurate MTF can be produced from a single exposure of a comprehensive phantom using clinical parameters (e.g., spectrum and dose). An alternative is the slit method,[8] but this requires large x-ray exposures which are often obtained by applying multiple exposures. High quality slit images are very difficult to obtain with flat-panel detectors due to these dose requirements. Theoretical analysis also showed that the SNR,[19] defined as the ratio of the MTF value to the standard deviation in an ensemble of MTF determinations from independent measurements, is highest at low frequencies for the edge method and highest at high frequencies for the slit method. As we are interested in an accurate measurement of the low frequency components, the use of the edge method seems preferable.

The present study was triggered by the following observations: First, we had previously implemented an algorithm to calculate the MTF for digital mammography applications with an edge device; however, we sought to definitively evaluate the accuracy of our approach and we could not find images readily available for calibration or intercomparison of our method with other methods. Second, the MTF as calculated by several groups from the same set of data gave very different results,[21] especially when the edge object was placed within 4 cm of PMMA to simulate the scatter of a real compressed breast. Third, the LFD typically observed in the MTFs acquired under clinical conditions is discussed in only a small subset of papers.[12–14,21]

In the first part of this paper we evaluated the accuracy of our MTF algorithm and considered the impact of several methods which have been cited as having the potential to improve MTF accuracy. We used simulated edge images for which the true MTF was known. These images contained simulated noise, scatter, and flat-field nonuniformities as observed in flat-field images obtained with various commercially available full-field digital mammography systems. We

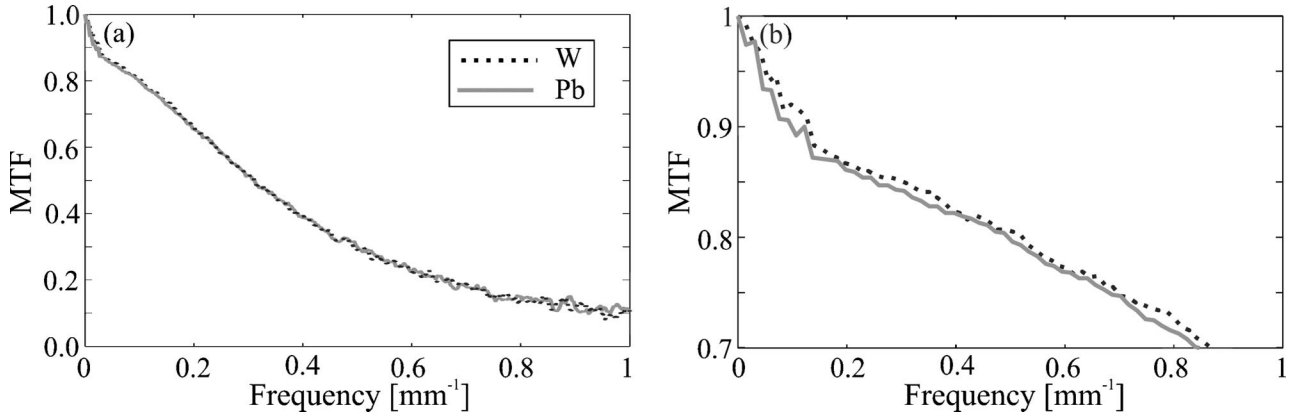

FIG. 15. Effect of the edge material on MTF. The measured MTFs of the edge device with the 5 cm by 5 cm W foil and the 5 cm by 5 cm Pb foil are shown. The ROIs to determine the supersampled ESF had length $L=71$ mm and width $W=46$ mm. A magnified region demonstrating the LFD is shown on the right.

showed that the MTF derived with our algorithm perfectly matches the theoretical MTF up to $1/2$ the sampling frequency for a synthetic edge image without noise, scatter or flat-field nonuniformities. The accuracy of the MTFs calculated with our algorithm was independent of the explored noise levels (50%–200% of the typical clinical dose). A larger noise level in the edge image led only to a larger variability of the calculated MTF.

The variability of the MTF decreased for larger width, W, of the ROI with our method. Larger W implies averaging over more supersampled ESFs and gives a smoother mean supersampled ESF (step 4 in Sec. II A). As discussed further in the following, very large values of W may introduce errors due to image nonuniformity. The variability of the MTF decreased for shorter length, L, of the ROI. This is because the variance of each Fourier component is proportional to the length of the supersampled ESF. As a result, truncating the tails (i.e., shorter L) is an approach that has been used to reduce the variability of the MTF. However, as mentioned in Refs. 1 and 19 the length of the LSF should be large enough to accurately estimate the MTF when scatter is present in the image. The necessary length of the ESF will depend on the amount of scatter in the edge image. In the present study, we simulated an edge image with a MTF that has a large LFD. This LFD is larger than those which we measured using an edge object placed within 4 cm PMMA for the 4 FFDM systems discussed in Ref. 22 (results not shown). These findings indicate that an edge profile of $L=56.5$ mm is sufficient for an accurate LFD estimation.

Various other methods have been explored to reduce the variability of the MTF.[6,7,9,19,20] As far as we know, there are no publications that report on the magnitude of the error associated with use of noise reduction methods when the MTF is calculated from images with a significant amount of scatter. We considered four different noise reduction techniques and evaluated their impact on the accuracy of the MTF calculated from a simulated edge image containing scatter. The techniques included applying a Hann window to the LSF, fitting the tails of the LSF to an exponential function, imposing a monotonic criterion to the ESF and applying a third-order low-pass filter to the MTF. The MTF variability was reduced with all techniques. But the monotonic criterion and the third-order low pass filter resulted in the most accurate MTFs. However, we have shown that a Hann window and a decaying exponential function may cause systematic overestimations of the low frequency components of the MTF. When applying a Hann window, the magnitude of the error decreases with increasing aperture size of the window. A similar reasoning holds for the position where the exponential fit through the LSF tails start; it may be appropriate to fit only tails which are slowly changing. Care should also be taken to avoid a discontinuity where the exponential fit starts, as this may result in Gibbs ringing.

Most MTF algorithms presume that the edge image has been flat-fielded prior to processing. This is unachievable when calculating the MTF in clinical conditions as not all detectors can be flat-fielded (e.g., CR plates). In applying a flat-field correction to clinical images, it must not introduce a bias in the MTF. There is a trade-off between the accuracy of the LFD and the sensitivity to flat-field nonuniformities.

In the second part of this paper, we made exposures of edge test objects with foils of different spatial extent and composition. We calculated the MTFs from acquisitions of these edge objects placed within 4 cm PMMA obtained with a FFDM system with a notable LFD. To minimize experimental errors, all measurements were performed with the same physical arrangement. These measurements are a first step in exploring how to accurately perform MTF measurements of digital mammography systems. A summary of our conclusions is presented here.

The size of the W foil, going from a 2.5 cm by 2.5 cm foil to a foil that covers half the detector, affected the MTF accuracy only slightly. The nonuniformity of the scatter at the periphery of the smallest edge device had an influence of less than 1% on the LFD. This scatter nonuniformity together with the length, L, of the supersampled ESF, which was chosen to be as long as possible given the small size of the edge, caused an overestimation of the LFD of less than 2%. These small errors confirm that small edges in a comprehensive

phantom are well suited for routine clinical applications as part of a quality control program, where reproducibility is especially important.

In the case where an accurate system MTF is desired, we therefore recommend the use of an edge of at least 5 cm by 5 cm, as this provides a better estimate of the LFD, but with the caveat that nonuniformities should be small and well understood.

The MTFs obtained from a nontransparent (W) and a partially transparent (Pb) edge were slightly different. The MTF of the Pb edge was up to 2% smaller in the low frequency range, an effect that can be understood by the L-fluoresence in Pb that introduces another contribution to the LFD. But, this difference may also partly be ascribed to defects in the edge, an effect that is difficult to verify.

There are many other factors that affect the accuracy of the MTF. We shall only mention one that we found to be important experimentally. The accuracy of the measurements may be affected if the edge foils do not have a uniform thickness. This causes the fraction of transmitted x rays through the edge foil to be spatially dependent. Thickness variations will cause larger inaccuracies in images of thin foils than in images of thicker foils.

In conclusion, our results underline the need for clear guidelines if the MTF is to be given a more crucial role in the acceptance of digital mammography systems. Specifically, the MTF algorithm and edge object test tool need to be publically validated.

ACKNOWLEDGMENT

We acknowledge the financial support of the European Breast Cancer Network.

[a]Electronic mail: ann-katherine.carton@uphs.upenn.edu

[1]ICRU Report 41, "Modulation transfer function of screen-film systems," 1986.

[2]C. E. Metz and K. Doi, "Transfer function analysis of radiographic imaging systems," Phys. Med. Biol. **24**, 1079–1106 (1979).

[3]The European Protocol for the Quality Control of the Physical and Technical Aspects of Mammography Screening: Addendum on Digital Mammography, September 2003.

[4]International Electrotechnical Commission, International Standard IEC 62220-1:2003-10, "Medical electrical equipment-characteristics of digital imaging devices. 1 Determination of the detective quantum efficiency," Geneva.

[5]International Electrotechnical Commission, International Standard IEC 62220-2: Draft version 2004-02, "Medical electrical equipment-characteristics of digital imaging devices. 1 Determination of the detective quantum efficiency," 2004.

[6]H. Fujita, D.-Y. Tsai, T. Itoh, K. Doi, J. Morishita, K. Ueda, and A. Ohtsuka, "A simple method for determining the modulation transfer function in digital radiography," IEEE Trans. Med. Imaging **11**, 34–39 (1992).

[7]E. Samei, M. J. Flynn, and D. A. Reimann, "A method for measuring the presampled MTF of digital radiographic systems using an edge test device," Med. Phys. **25**, 102–113 (1998).

[8]J. Dobbins, "Image quality metrics for digital systems," in *Handbook of Medical Imaging*, Physics and Psychophysics Vol. 1, edited by J. Beutel, H. L. Kundel, and R. L. Van Metter (SPIE, Bellingham, WA, 2000).

[9]A. D. A. Maidment and M. Albert, "Conditioning data for calculation of the modulation transfer function," Med. Phys. **30**, 248–253 (2003).

[10]K. A. Fetterly and B. A. Schueler, "Performance evaluation of a dual-side read dedicated mammography computed radiography system," Med. Phys. **30**, 1843–1854 (2003).

[11]E. Buhr, S. Günther-Kohfahl, and U. Neitzel, "Accuracy of a simple method for deriving the presampled modulation transfer function of a digital radiographic system from an edge image," Med. Phys. **30**, 2323–2330 (2003).

[12]F. Rogge, D. Vandenbroucke, L. Struye, H. Bosmans, P. Willems, and G. Marchal, "A practical method for detected quantum efficiency (DQE) assessment of digital mammography systems in the radiological environment," Proc. SPIE **4682**, 645–655 (2002).

[13]F. Rogge, H. Bosmans, P. Willems, and G. Marchal, "The use of MTF calculation in global and local resolution assessment in digital mammography," Proc. SPIE **5030**, 896–907 (2003).

[14]S. Z. Shen, G. E. Mawdsley, A. K. Bloomquist, J. G. Mainprize, and M. J. Yaffe, "Interpreting system MTF and NPS measured on clinical digital mammography systems," Proceedings of the Workshop IWDM 2002, Bremen, Germany, 22–25 June 2002, pp. 123–127.

[15]F. O. Bochud, J. F. Valley, F. R. Verdun, C. Hessler, and P. Schnyder, "Estimation of the noisy component of anatomical backgrounds," Med. Phys. **26**, 1365–1370 (1999).

[16]P. B. Greer and T. van Doorn, "Evaluation of an algorithm for the assessment of the MTF using an edge method," Med. Phys. **27**, 2048–2059 (2000).

[17]J. Terry, R. G. Waggener, and M. A. Miller Blough, "Half-value layer and intensity variations as a function of position in the radiation field for film-screen mammography," Med. Phys. **26**, 259–266 (1999).

[18]P. J. R. Leblans, P. Willems, and L. B. Alaerts, "New needle-crystaline detector for x-ray computer radiography," Proceedings of the Eighth European Conference on Nondestructive Testing, Barcelona, Spain, 17–21 June 2002, accessed at http://www.ndt.net/article/ecndt02/44/44.htm (March 2005).

[19]I. A. Cunningham and B. K. Reid, "Signal and noise in modulation transfer function determinations using the slit, wire, and edge techniques," Med. Phys. **19**, 1037–1044 (1992).

[20]F. Judy, "The line spread function and modulation transfer function of a computed tomographic scanner," Med. Phys. **3**, 233–236 (1976).

[21]F. Rogge, H. Bosmans, and G. Marchal, "Practical MTF calculation in digital mammography: A multicenter study," Proc. SPIE **5368**, 761–769 (2004).

[22]A.-K. Carton, "Development and application of methods for the assessment of image quality and detector performance in digital mammography," Ph.D. thesis.